

Performance and Development of a Miniature Rotary Shaft Pump

Danny Blanchard

Phil Ligrani¹

e-mail: ligrani@mech.utah.edu

Bruce Gale

Department of Mechanical Engineering,
University of Utah, 50 South Central Campus
Drive, Rm. 2110, Salt Lake City, UT 84112

The development and performance of a novel miniature pump called the rotary shaft pump (RSP) is described. The impeller is made by boring a 1.168 mm hole in one end of a 2.38 mm dia shaft and cutting slots in the side of the shaft at the bottom of the bored hole such that the metal between the slots defines the impeller blades. The impeller blades and slots are 0.38 mm tall. Several impeller designs are tested over a range of operating conditions. Pump performance characteristics, including pressure rise, hydraulic efficiency, slip factor, and flow rate, are presented for several different pump configurations, with maximum flow rate and pressure rise of 64.9 ml/min and 2.1 kPa, respectively, when the working fluid is water. Potential applications include transport of biomedical fluids, drug delivery, total analysis systems, and electronics cooling.

[DOI: 10.1115/1.1949641]

Introduction

The area of microfluidics is developing with many new sensors, separation devices, drug delivery systems, and other small-scale and microscale fluidic devices. For many of these devices there is a need to circulate or move fluid through macro and microscale channels. A variety of micropumps are available to meet this need, generally to fulfill specific applications [1]. These include membrane pumps [2–8] (both without check valves [2–5] and with check valves [6–8]), electrohydrodynamic (EHD) pumps [9–11], electrokinetic (EK) pumps [12,13], rotary pumps [14–18], peristaltic pumps [4,19–21], ultrasonic pumps [22,23], and several other types of pumps [24–27]. Other small-scale pumps have been developed for uses as blood pumps in ventricular assist devices [28–30]. Nonmechanical pumps, such as the electrohydrodynamic and electrokinetic pumps, do not have moving parts, which increases reliability. However, such devices are generally limited by low flow-rate and pressure-rise capabilities, the applications of the pump, the working fluids that can be pumped, and high supply voltage requirements [1]. Mechanical pumps, such as rotary, peristaltic, and membrane pumps, have a wide variety of possible working fluids and applications. However, such mechanical micropumps (such as rotary micropumps) are believed to be feasible only when they are greater than a certain size [1].

One motivation of the present effort is to demonstrate the operation and feasibility of a millimeter-scale pump, which imposes fluid motion and pressure rise by means of viscous and inertial forces. The behavior and performance of macroscale centrifugal pumps are well established and well known. However, the dynamics, performance, and efficiency of centrifugal pumps change as the size of the pump is altered. For example, secondary flows, and the losses associated with them, become more important as macroscale impeller passage size decreases. As size decreases further, surface (viscous) forces become more significant [31] and can dominate the performance of the pump. However, this does not appear to prevent the operation of the centrifugal micro- and minipumps developed by Ahn and Allen [17] and Hainan et al. [14]. The micropump by Ahn and Allen [17] is a radial-inflow–radial-outflow design and is powered by an integrated magnetic micromotor with a 12 pole, 500 μm dia stator that also acts as the impeller. The advantage of this pump is the integrated magnetic motor, which also serves as a completely sealed pumping chamber with no leaks. This pump reaches a maximum flow rate of

24 $\mu\text{l}/\text{min}$, with a maximum theoretical pressure rise of 100 Pa. The mini-pump by Hainan et al. [14] is a centrifugal pump with an axial inflow and a radial outflow configuration. This pump is created using precision machining techniques and measures 6 mm \times 12 mm. This axial-inflow–radial-outflow pump produces a maximum flow rate of 100 ml/min, with a maximum pressure rise of 10 kPa. One disadvantage of this micropump is the potential leakage at the shaft-pump housing interface, which creates losses and reductions in performance. Even though some flow conditions are provided, extensive performance data for these pumps are not provided, nor are any details given regarding efforts to optimize the pump and impeller designs.

The present paper presents a novel rotary pump (shown schematically in Fig. 1), which has a 2.38 mm dia impeller and relatively high hydraulic efficiency at low flow rates. The design modifications [32], relative to other small-scale centrifugal devices, include the impeller integrated into the body of the shaft, instead of on the top of the shaft. This design is unique and novel because of its simplicity, which allows it to be easily manufactured at low cost, and because all problems of tip blade clearance and flow leakage around the blade tips are not present. Pump performance is characterized since the pressure rise, flow rate, and the hydraulic efficiency are given for a wide range of impeller speeds and impeller configurations. Tested impeller designs include radial two-, four-, and six-blade; backward-curved four-blade; and forward-curved four-blade arrangements. The fluid flow for each impeller design is throttled using outlet tubing inner diameters of 0.254, 0.508, and 1.397 mm of the same length, or by placing a valve at the end of the 1.397 mm outlet tubing. The present pump, or a variation of it, is useful for a variety of microbiological and biomedical analysis systems, electronics cooling, and drug delivery devices. For example, a larger-scale version of this pump has potential use as a blood pump for a ventricular assist device.

Pump Configuration and Geometry

One important dimension of many centrifugal pumps is the gap distance between the tips of the blades and the pump housing. As the gap increases, there is more leakage across blades and the overall hydraulic efficiency of the pump decreases. If the gap is too small or zero, then the blades can be damaged by contacting the pump housing. On a macroscale, this “gap problem” is generally insignificant, but on a microscale, or a millimeter-scale, the gap between the tips of the blades and the pump housing can be about the same as the height of the impeller blades.

The design of the rotary shaft pump (RSP) eliminates this “gap problem.” The RSP impeller is constructed by boring a hole in the

¹Author to whom correspondence should be addressed.

Contributed by the Fluids Engineering Division for publication in the JOURNAL OF FLUIDS ENGINEERING. Manuscript received by the Fluids Engineering Division April 21, 2004; final manuscript received April 15, 2005. Associate Editor: Akira Goto.

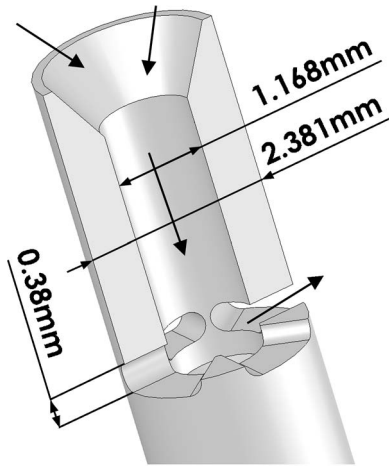


Fig. 1 Cutaway view of the rotary shaft pump (RSP) impeller. Shown is the radial four-blade impeller. Arrows indicate flow direction.

end of a shaft and then cutting slots in the side of the shaft at the bottom of the bored hole as shown in Fig. 1, which presents a cutaway view of the RSP impeller. Thus, the metal between the slots acts as the blades of the impeller, and the slots form passages between the bored interior and outer shaft surface. The gap at the tip of the blades is zero because the tips of the blades also connect to the shaft.

The rotating shaft is mounted using bearings located above and below the exit plenum, which are mounted in the pump housing. The volute and an outlet channel are then located in the region between the upper and lower bearings and pump housing, as seen in Fig. 2. The water reservoir is connected to the pump housing by a plastic tube with an inner diameter of 4.5 mm and length of 381 mm. This plastic tube is press fit into the inlet channel as shown in Fig. 2. There is a continuous channel, from the inlet tubing, through the pump housing and top of the upper bearing, to the inlet of the RSP. Inside the channel through the upper bearing, the fluid flow transitions from a nonrotating bearing wall to the inside of a rotating shaft. The bearing forms a seal for the spinning shaft of the RSP, which reduces the leakage from the impeller outlet to the shaft inlet of the RSP. The sidewalls of the volute and part of the outlet channel are formed by a piece of machined brass shim stock that is 416 μm tall. This volute and outlet channel is aligned with the slot ports of the shaft. With this construction, when the shaft spins, centrifugal forces from the spinning impeller shaft forces fluid flow through the shaft inlet, through the interior of the shaft, through the slots, out through the slot ports, into the volute,

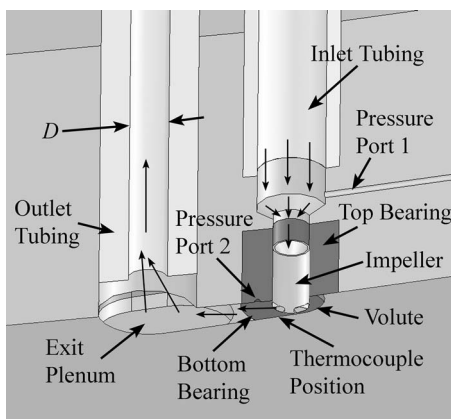


Fig. 2 Cutaway view of the RSP assembly

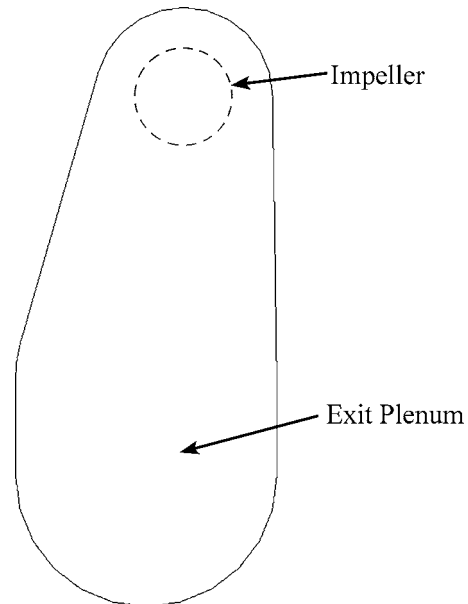


Fig. 3 Open volute configuration

and then into and through the outlet channel, as shown by the arrows in Figs. 1 and 2. The volute design employed for the present investigation, to minimize the effects of surface forces, is called the open volute design. The open volute design is characterized by a large “open” channel from the impeller to the exit plenum, as shown in Fig. 3.

One of the purposes of a volute is to efficiently direct fluid toward the outlet channel. The volute designs employed in macroscale pumps, where fluid motion is induced by inertial forces, are different from the design employed here. This design difference is because flow from the impeller exit and within the volute is significantly influenced by both inertial forces and surface forces. The present open volute design increases the width and maximizes the hydraulic diameter thereby decreasing the average fluid velocity and velocity gradients, which also reduces viscous losses.

Pump Component Fabrication

There are five main fabricated components of the rotary shaft pump assembly: (i) the impeller, (ii) top housing, (iii) bottom housing, (iv) bearings, and (v) volute.

Fabrication of the impeller is realized using precision machining techniques. A lathe is used to obtain the desired outside diameter of the shaft and to bore the hole in the end of the shaft. The cone shape at the inlet of the shaft is made using a center drill. Slots are then cut into the side of the shaft using a milling machine and an indexing tool. The impeller is made from 304 stainless steel. Five impeller designs are constructed for testing: radial two-, four-, and six-blade; backward-curved four-blade; and forward-curved four-blade. The blades are evenly spaced around the circumference of the shaft. The blades on the impellers are 0.38 mm tall (the slots are 0.38 mm tall). The geometry of the backward-curved four-blade impeller is shown in Fig. 4. The geometry of the other impellers is shown in Fig. 5. The backward-curved four-blade impeller has β_1 and β_2 angles of 80 and 85 deg, respectively. The forward-curved four-blade impeller has β_1 and β_2 angles of 144 and 114 deg, respectively.

The top housing is made from acrylic to allow the flow passing into and through the pump to be visualized. The top housing has an inlet channel and outlet channel, as seen in Fig. 2, and also has two pressure ports. The first pressure port is connected to the inlet channel passage, as seen in Fig. 2, and is just above the upper bearing at the inlet to the top of the rotary shaft pump. The second

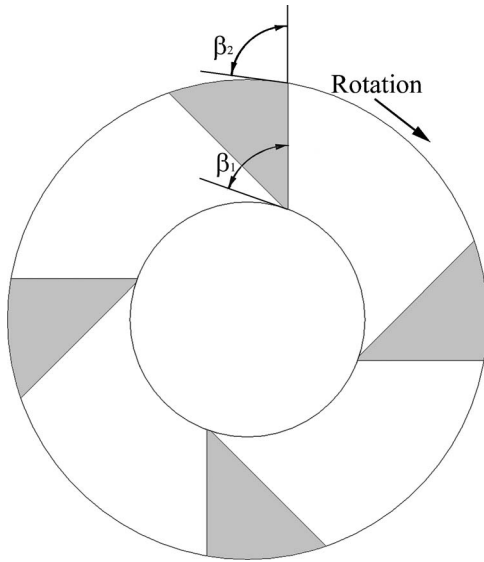


Fig. 4 Impeller blade configuration and angles. Impeller shown is the backward-curved four-blade impeller.

pressure port is connected to part of the volute and comes through the upper bearing into the volute region about 2 mm from the outer surface of the shaft. The diameter of the pressure ports at the fluid channel interface is ~ 0.4 mm. Each of these then expands to 3.1 mm. The ends of clear plastic tubes are press fit into the 3.1 mm dia holes, and the opposite ends of the tubes are connected to opposite sides of the differential pressure transducer (which is described later). Thus, the pressure transducer measures the differential pressure between the two pressure ports. The bottom housing is made from aluminum and contains the lower bearing. The bottom housing also has a recess that forms the exit plenum. The expansion of the fluid channel as it enters the exit plenum slows the fluid and minimizes losses as the fluid turns to the outlet channel.

The bearings are made from Torlon, a strong self-lubricating plastic. The upper and lower bearings are press fit into the top and bottom housing, respectively. Torlon is used because it has a low coefficient of friction and can be easily machined. The outer di-

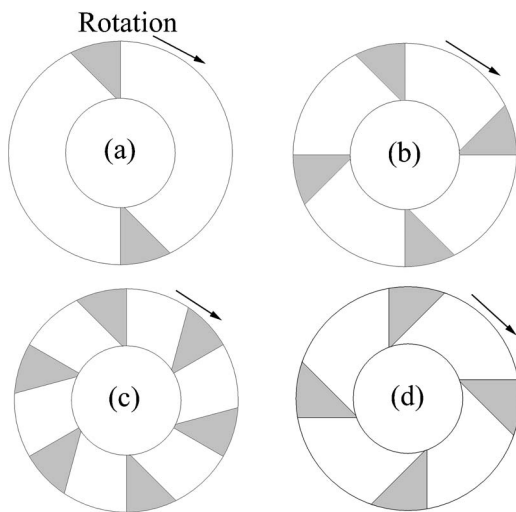


Fig. 5 Impeller blade configurations for the (a) radial two-blade, (b) radial four-blade, (c) radial six-blade, and (d) forward-curved four-blade impellers

ameter of the bearings is 6.35 mm, and the inner diameter is 2.38 mm. The locations of these bearings are shown in Fig. 2.

The volute is machined from brass shim stock using a computer numerically controlled (CNC) milling machine and is positioned and designed as seen in Figs. 2 and 3. Each piece of brass shim stock is $104 \mu\text{m}$ thick. Thus the height of the volute can be changed by stacking pieces of brass shim stock. For all the present tests, a height of 0.416 mm is used because it is just larger than the height of the slots located in the shaft.

Pump Performance

Parameters that characterize pump performance include head pressure rise, volumetric flow rate, overall slip factor magnitude, and hydraulic efficiency. The Euler equation relates pumping head to impeller geometry, speed of the impeller, and the flow rate of the fluid [33]. For the impeller configuration shown in Fig. 4, this equation is given by

$$H_{th} = \frac{1}{g}(U_2 C_{u2} - U_1 C_{u1}) \quad (1)$$

With the present impeller arrangement, shown in Figs. 1 and 2, the rotating hollow interior of the RSP transfers momentum to the passing fluid through viscous forces. This “preswirl” can be significant on a millimeter- or micrometer-scale, especially when the ratio of the hollow interior length to diameter is large and the circumferential wall velocity is greater than the average axial fluid velocity. The preswirl may aid the overall pumping process by reducing the sudden acceleration of the fluid at the inner blade tip, which may reduce the flow separation near the leading edge of the impeller blade. Tangential components of absolute velocity are also induced at the inlets of the slots that make up the pump impeller. The spatially averaged magnitude of this tangential fluid motion can be characterized using αU_1 . The contribution to theoretical head is then contained in the last term of Eq. (1), which can then be expressed using $U_1 C_{u1} = \alpha U_1^2$. This imposed inlet swirl then reduces the work required by the impeller blades, for a particular magnitude of induced overall pressure rise for the pump.

In general, even though some local swirling motions may be induced near the slot inlets, the overall effects of the inlet swirl on the present pump configuration are believed to be relatively small, and so they are neglected to give $\alpha \approx 0$ and $C_{u1} = 0$. The Euler equation, with no inlet preswirl, or no prerotation of the fluid at the inlet of the impeller, is then employed to analyze the present experimental data. The corresponding form of this theoretical head equation is given by

$$H_{th} = \frac{1}{g}(U_2 C_{u2}) \quad (2)$$

Fluid slip is present when the actual tangential component of absolute velocity of the flow at the impeller exit C_{u2} deviates from the ideal value ($C_{u2,i}$) given by the outlet blade angle β_2 [34] as given by

$$C_{u2,i} = U_2 - \frac{\cot(\beta_2)Q}{\pi D_2 h} \quad (3)$$

Slip thus occurs when the flow through the pump deviates from the exact contours of the impeller blades [34]. In the present study, a slip velocity and a slip factor are employed that are defined using equations of the form [35]

$$v_{\theta s} = C_{u2,i} - C_{u2} \quad (4)$$

and

$$\sigma = 1 - \frac{v_{\theta s}}{U_2} \quad (5)$$

Substituting Eqs. (3)–(5) into Eq. (2) then gives an equation for the theoretical pumping head [35], which can be written as

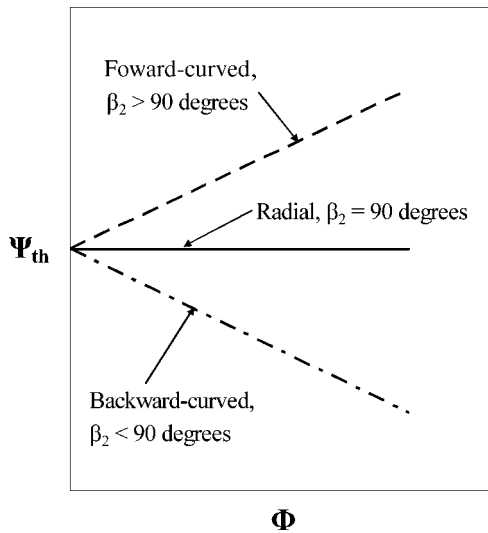


Fig. 6 Idealized trends of nondimensional pump head and nondimensional flow rate for different impeller designs

$$H_{th} = \sigma \frac{U_2^2}{g} - \frac{U_2 \cot(\beta_2) Q}{\pi D_2 h g} \quad (6)$$

The slip factor thus provides a means to relate volumetric flow rate (Q) to Euler or theoretical head H_{th} . Although the actual pumping head H_{act} is given by subtracting the flow losses from H_{th} , the actual $Q-H_{act}$ characteristics are often well represented by $Q-H_{th}$ characteristics, especially when the flow losses are relatively small. With radial impeller designs, $\beta_2=90$ deg and the second term in Eq. (6) is zero. For the corresponding impeller configuration shown in Fig. 5 (with constant rotational speed), the nondimensional theoretical head (Ψ_{th}) is constant as the flow rate increases and represented by the horizontal line in Fig. 6. With forward-curved impeller designs, $\beta_2 > 90$ deg, and constant speed, Fig. 6 shows that nondimensional theoretical head increases as the flow rate increases. Backward-curved impeller designs have $\beta_2 < 90$ deg, and the nondimensional theoretical head decreases as flow rate increases for constant impeller rotational speed, which is also illustrated in Fig. 6. Here, the flow rate and head are normalized using the equations given by

$$\Phi = \frac{4Q}{\pi D_2^2 U_2} \quad (7)$$

and

$$\Psi = \frac{Hg}{U_2^2} \quad (8)$$

Note that Ψ can be given either in terms of H_{th} or H_{act} , which leads to Ψ_{th} and Ψ_{act} respectively.

In the present investigation, the slip factor correlation proposed by Wiesner [36] is used to determine σ magnitudes in the RSP impellers. This correlation is given by

$$\sigma = 1 - \frac{\sqrt{\sin \beta_2}}{n^{0.7}} \quad (9)$$

Slip-factor correlations proposed by Stodola [37], Stanitz [38] and Paeng and Chung [39] are not employed because the values produced from these correlations are unrealistic and unreasonable for the RSP impellers tested.

The actual measured head H_{act} , measured between the pump inlet and outlet (described earlier), is generally less than the theoretical head given by Eq. (6) since H_{th} represents the work imposed onto the fluid around the circumference of the pump impel-

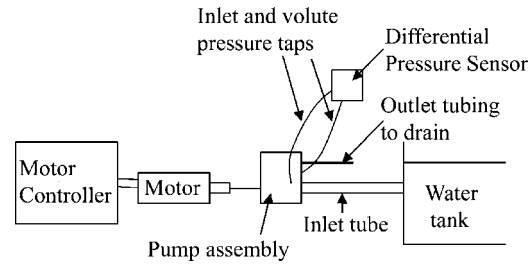


Fig. 7 Experimental testing apparatus. Differential pressure sensor measures pressure rise across the pump. Motor controller has an output signal for shaft speed and motor current.

er. The actual measured head (H_{act}) is based on the fluid density, gravitational constant, and the pressure measurements made at pressure ports 1 and 2 (shown in Fig. 2), and is given by

$$H_{act} = \Delta P / \rho g \quad (10)$$

Hydraulic efficiency accounts for the flow losses in the volute between the circumference of the pump impeller and locations at the pump inlet and outlet. As such, hydraulic efficiency relates H_{th} and H_{act} and is determined using

$$H_{act} = H_{th} \eta_H \quad (11)$$

With the slip factor, the hydraulic efficiency is then a useful parameter for characterizing the performance of the different impeller designs, volute arrangements, and pump configurations. The Wiesner [36] slip-factor correlation is widely used for macroscale centrifugal impellers and also provides viable representations of physical behavior for micro and miniscale pumps. The Wiesner slip correlation is employed for analysis of the miniscale pumps of the present study because most other slip-factor correlations [37–39] give values that are physically implausible.

Experimental Apparatus and Procedures

The rotary shaft pump is powered by an externally mounted Maxon EC32 number 118891, brushless DC motor that is 32 mm in diameter, with an 80 W power rating. The maximum speed is 25,000 rpm, with a stall torque of 0.35 N-m. The maximum testing speed is limited by the maximum speed of the optical encoder (16,000 rpm) attached to the motor shaft. The motor has a torque constant of 7.45 mN-m A^{-1} and a voltage constant of 1281 rpm V^{-1} . The brushless motor is controlled by an Advanced Motion Controls power amplifier (Model #BE12A6). The power amplifier has a DC supply voltage of 40 V, a peak current of 12 A, and continuous current rating of 6 A. A negative feedback controller is employed to maintain constant speed for any variation in torque. The speed is controlled by adjusting a 15-turn potentiometer. The speed range is 100–15,300 rpm. The motor controller determines the rotational speed from the signal from an optical encoder attached to the motor shaft. This apparatus produces a voltage signal that is proportional to speed and one that is proportional to motor current. These voltages are measured using a Keithley 131 Digital Multimeter.

The test setup is shown in Fig. 7 and includes a water reservoir, which is large enough that the water-level change during operation is negligible. The outlet channel is connected to the outlet tubing. All outlet tubing is a constant length of 89 mm. The inside diameters of the outlet tubing are changed to throttle the outflow of the rotary shaft pump. The outlet tubing inside diameters (D) are 0.254, 0.508, 1.397, and 4.5 mm. The outflow of the RSP is also throttled using a valve at the exit of the 1.397 mm outlet tubing. The pump housing is mounted to the base of a linear slide. The brushless motor and coupling shaft are mounted to the shuttle of the linear slide. The coupling shaft is used to connect the impeller shaft with the motor shaft. The coupling shaft is made from aluminum and is secured by ball bearings at each end. The rotary

shaft pump impeller shaft is connected to the coupling shaft. The position of the shuttle, along with the motor and impeller shaft, are adjusted and secured using 4-40 positioning bolts. There is one positioning bolt at each of the two ends of the shuttle, such that one positioning bolt is used to adjust the position and the other is used to immobilize the shuttle. A microscope is used to aid the positioning of the impeller shaft by means of the positioning bolts. The microscope is an Infinear Continually-Focusable Microscope (CFM) (0-330X magnification), manufactured by Infinity Photo-Optical Co., with a Hitachi HV-C20U-S4 video camera connected to a Sony Tinitron PVM-14N5U high-resolution monitor.

The pressure ports in the pump housing, shown in Fig. 2, are connected to a DP-15 differential Validyne pressure sensor through two tubes. The pressure-sensor diaphragm used in this transducer has a full range of 0–3.5 kPa. The range of pressure measurements during testing is 0–2.1 kPa. The output signal from the pressure sensor is processed using a Celesco Model No. CD10D Carrier Demodulator, which produces a voltage output that is proportional to pressure. The voltage is measured by a Keithley 131 Digital Multimeter.

A type-T thermocouple made by Omega Engineering Inc. (Part No. TT-T-36-SLE) is used in several experiments to determine the temperature rise through the impeller. Figure 2 shows that the thermocouple is positioned next to the sidewall of the volute, about 2 mm from the outer surface of the shaft. The signal from the thermocouple is measured by an HP 3497A data acquisition control unit that electronically compensates for a reference voltage level at 0 °C. Temperature measurements indicate that the water temperature increases 1–2 °C while traveling through the impeller for rotational speeds of 1000–15,300 rpm. Because of the small range in temperature rise, the condition of constant fluid properties is a good assumption for the water employed as the working fluid.

Pump assembly starts by connecting the impeller shaft to the coupling shaft on the motor. The bottom housing is then mounted to a plate on the face of the linear slider, and the position of the slots is adjusted so that the bottom of the slots is flush with the top surface of the bottom housing. The volute is positioned and secured in place. The top housing is secured and tightened to minimize leakage. The inlet and outlet tubes are then connected to the top housing. After assembly and positioning of the impeller shaft and housing, all the air is bled from the system using a syringe attached to the end of the inlet tubing. This includes the inlet channel, outlet channel, and tubing to and from the pressure sensors. After these steps are completed, testing is comprised of the following procedures: (i) The system is flushed to ensure there are no air bubbles or trapped particulates in the pumping chamber; (ii) the pump motor is activated and adjusted to produce the desired speed; (iii) the pump then continues to operate at constant speed until steady state is reached, which usually requires 20–30 s, and (iv) the timer is started, and water from the outlet tubing is collected. Output signals related to shaft rotational speed, motor current, pressure rise, and volumetric flow rate are then collected. The volumetric flow rate is determined by dividing the amount of water collected by the collection time. The motor torque is determined by multiplying the motor current obtained from the motor controller by the torque constant of the motor. All data are recorded, and then entered and processed using a Dell Latitude laptop computer with a 1.15 GHz Pentium III processor, 256 MB RAM, with a Microsoft Windows XP Professional operating system, and Microsoft Excel XP software.

Experimental Uncertainty Analysis

A first-order uncertainty analysis is performed using constant-odds combination method, based on a 95% confidence level as described by Moffat [40]. Table 1 presents uncertainties associated with experimental data. The uncertainty is greatest at low

Table 1 Uncertainties associated with experimental data

Variable	Percent uncertainty at 2640 rpm	Percent uncertainty at 7920 rpm	Percent uncertainty at 15,300 rpm
H_{th}	5	2.5	2
H_{act}	15	3	1
η_H	15	3	2
Q	2	2	2
T	10	5	2

rotational speed, and pressures, due to the small signal to uncertainty ratios. The uncertainty decreases significantly as the rotational speed and pressure increase.

Results and Discussion

The experimental results are presented in three sections. The first section discusses head and flow-rate variations for the radial two-, four-, and six-blade; backward-curved four-blade; and forward-curved four-blade impeller configurations for a constant rotational speed. The second section discusses the performance characteristics of the radial six-blade and the backward-curved four-blade impellers over a range of rotational speeds. Here, each impeller design is tested using outlet tubing diameters of 0.254, 0.508, 1.397, and 4.5 mm of the same length or by partially closing a valve located at the exit of the outlet tubing with a 1.397 mm i.d. The third section discusses the slip factor and hydraulic efficiency of all the rotary shaft pump (RSP) impellers.

Trends for Different Impeller Designs. The variations of idealized nondimensional head with nondimensional volumetric flow rate for macroscale pumps with different impeller blade configurations are shown in Fig. 6. Figure 8 shows actual nondimensional head with nondimensional flow rate for different RSP impeller designs, all for an impeller rotational speed of 10,710 rpm. To obtain the data presented in Fig. 8, the flow is throttled in the rotary shaft pump experiments by changing the inside diameter of the outlet tubing, or by partially closing a valve located at the exit of the outlet tubing with a 1.397 mm inner diameter. All outlet tubing is a constant length of 89 mm. The flow circuit determines the head requirements for a given flow rate through the tubing and pump and can be determined using the Darcy friction factor and

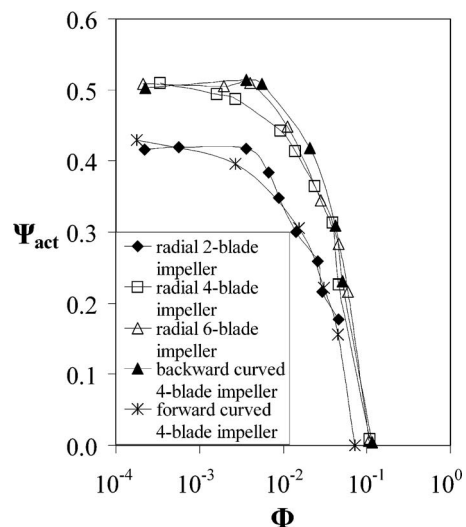


Fig. 8 Variation of nondimensional pumping head with nondimensional volumetric data for different impeller designs, where each data set is obtained at a constant impeller rotational rate of 10,710 rpm

minor loss correlations for expansions and contractions [33]. By decreasing the outlet tubing diameter, with constant length, the flow resistance out of the pump is changed, which changes the pressure rise and flow rate for a constant rotational speed. This arrangement is thus used to provide information on the performance of the rotary shaft pump over a range of rotational speeds, flow rates, and pressure rises.

For each impeller configuration (operating at constant impeller rotational speed), Fig. 8 shows that increasing the exit tube diameter, or more fully opening the exit valve, gives a higher volumetric flow rate through the pump, which, for the impellers tested, gives lower magnitudes of nondimensional head for flow rates greater than 5 ml/min. Qualitative trends of Fig. 8 data for each impeller configuration (at constant impeller rotational speed) are similar for $Q > 5$ ml/min, or $\Phi > 0.014$. Here, different data sets have similar slopes, sometimes with different ranges of pump head. At lower volumetric flow rates, data sets for different impeller configurations sometimes show completely different slopes, as well as different quantitative trends. Overall, data trends shown in Fig. 8 are similar to ones also observed at impeller rotational speeds of 1530 and 15,300 rpm.

Pumping head magnitudes produced by the impeller generally decrease as the flow rate is increased (as outlet tubing diameter increases) for a constant rotational speed. For the backward-curved four-blade impeller, one contributor for the head reduction at higher flow rates is the reduction in Euler work due to the increasing relative velocity at the exit of the impeller. For the forward-curved four-blade impeller, the Euler work should increase with increased flow rate, and therefore the lower head generation at higher flow rates suggests much higher flow losses compared to the backward-curved impeller. Note that for a volumetric flow rate of $Q = 10$ ml/min = 1.66×10^{-7} m³/s, the average fluid velocity in the 1.168 mm bored hole of the RSP impeller is 0.156 m/s. The head reduction at higher flow rates is also associated with a decrease of hydraulic efficiency, which is related to overall impeller behavior, and to increased hydrodynamic losses as flow rate increases. This is discussed further later in the paper.

Performance Characteristics of Pumps with Backward-Curved Four-Blade and Radial Six-Blade Impellers. Figures 9(a) and 9(b) show the non-dimensional variation of actual head with flow rate for the radial six-blade impeller and for the backward curved four-blade impeller, respectively, for different rotational speeds. The flow rate for each rotational speed is varied by using outlet tubing with inner diameters of 0.254, 0.508, 1.397, and 4.5 mm of the same length or by partially closing a valve located at the exit of the outlet tubing with a 1.397 mm I.D. As the rotational speed is increased, the dimensional head and flow rate also increase for each configuration. Note that the nondimensional Φ - Ψ_{act} data curves for the different impeller speeds tested are similar.

From Figs. 9(a) and 9(b), the maximum nondimensional flow rate obtained for both impeller configurations is about $\Phi = 0.127$, or $Q = 64.9$ ml/min at a rotational speed of 15,300 rpm. This maximum flow rate is obtained with an outlet tubing inner diameter of 4.5 mm. The maximum nondimensional head obtained at a rotational speed of 15,300 rpm is about $\Psi_{act} = 0.577$, or $H_{act} = 2.1$ kPa for both impeller configurations. Note that greater pressure rises and greater flow rates are present at higher rotational speeds.

The data given in Fig. 9 are given for the backward curved four-blade impeller and the radial six-blade impeller because these produce the highest pressure rise at a particular flow rate and also have the highest hydraulic efficiency at a particular volumetric flow rate. Of the pumps tested, the best millimeter-scale pump has backward-curved blades, and 4–6 impeller blades.

Figures 10 and 11 show the dimensional actual head and flow rate as they depend on rotational speed for the radial six-blade impeller and for the backward curved four-blade impeller, respec-

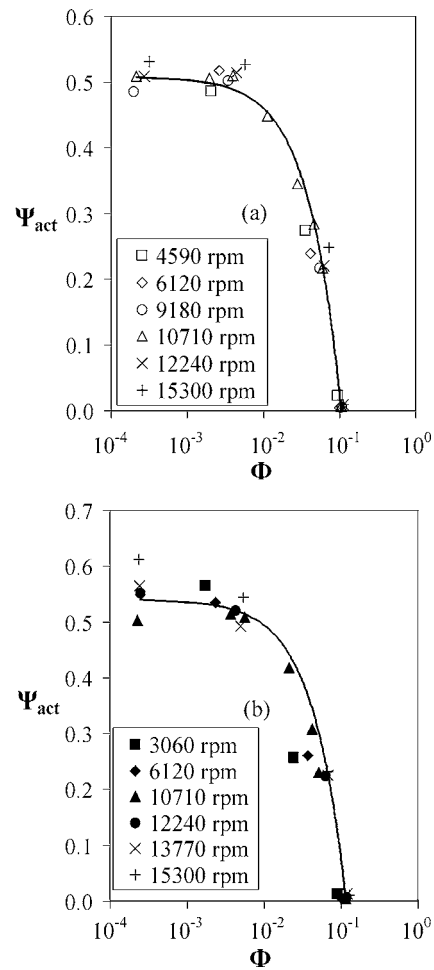


Fig. 9 Nondimensional pressure-rise and flow-rate data for the (a) radial six-blade and (b) backward-curved four-blade impellers for different rotational speeds. Flow rate is varied by using outlet tubing of different inner diameter from 0.254 to 4.5 mm, or by partially closing a valve on the end of the 1.397 mm outlet tubing.

tively. The data shown in Figs. 10 and 11 are obtained using rotational speeds from 1530 to 15,300 rpm and outlet tubing inner diameters of 0.0254, 0.508, and 1.397 mm of the same length. From the data presented, it is apparent that the flow rate can be changed easily by adjusting the rotational speed of the impeller and by changing outlet tubing diameter and length.

Hydraulic Efficiency and Slip Factor for All Impeller Configurations. Figure 12 shows hydraulic efficiency and nondimensional flow-rate variations for all the tested impellers. The data shown in Fig. 12 is a combination of all experimental data taken at rotational speeds between 1530 and 15,300 rpm and with the different outlet tubing diameters. Note that all hydraulic efficiency values are determined without accounting for any inlet swirl. Table 2 shows the slip factor magnitudes for the different impeller configurations. Note that the slip factor correlation from Eq. (9) gives values that are independent of flow rate and rotational speed. In Fig. 12, overall, the hydraulic efficiency decreases as flow rate increases. This is tied to impeller performance at higher flow rates. Note that greater viscous stresses are also present at higher flow rates because of larger velocity gradients. The maximum value of hydraulic efficiency is 0.87, which is obtained with the backward-curved four-blade impeller at a flow rate of $Q = 0.12$ ml/min, or $\Phi = 2.35 \times 10^{-4}$. The average magnitude of η_H decreases by 57% for the backward-curved four-blade impeller

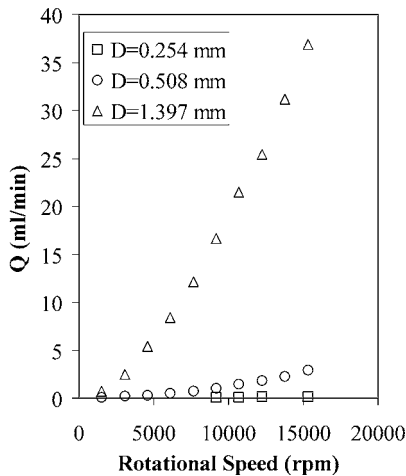
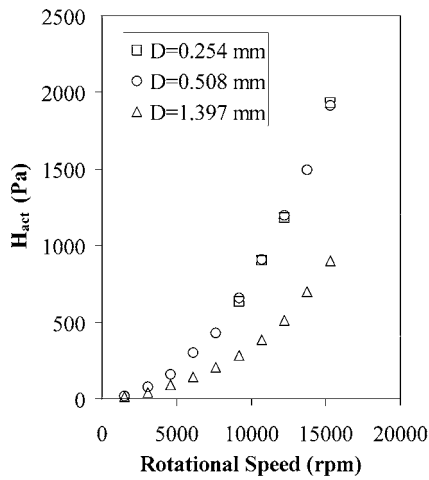


Fig. 10 Pressure-rise and flow-rate data for different rotational speeds for the radial six-blade impeller. Data are taken with impeller rotational speeds from 1530 to 15,300 rpm.

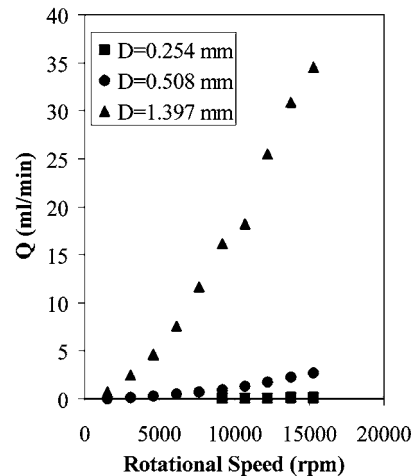
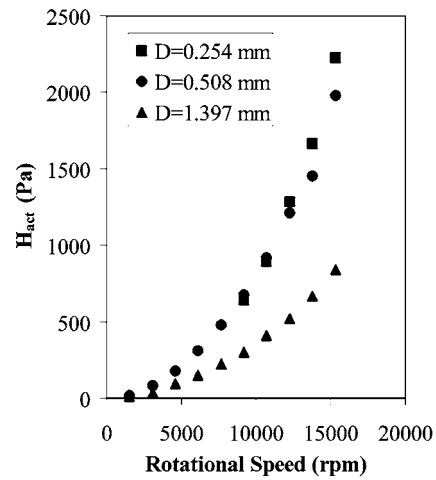


Fig. 11 Pressure-rise and flow-rate data for different rotational speeds for the backward-curved four-blade impeller. Data are taken with impeller rotational speeds from 1530 to 15,300 rpm.

as the flow rate increases to $Q=34.5$ ml/min or $\Phi=0.068$. There is also a difference of 22% in the average magnitude of η_H between the backward-curved and forward-curved four-blade impellers at flow rates of <5 ml/min. This implies that both the impeller design and flow rate are significant, but the flow rate has a more significant effect on the performance of the rotary shaft pump. Also, note that the motor torque increases from 2.7 to 4.5 mN-m as the rotational speed increases from 1530 to 15,300 rpm for the backward-curved four-blade impeller. Similar changes of motor torque are observed for all impeller blades tested for the same rotational speeds.

The most efficient impeller configurations are the radial six-blade and backward-curved four-blade impellers. The impeller configurations with the lowest hydraulic efficiency are the radial two-blade and forward-curved four-blade impellers.

Summary and Conclusions

A novel millimeter-scale rotary micropump called the rotary shaft pump (RSP) is developed, characterized, and tested. The top and bottom of the impeller blades of this device are integral parts of the rotary shaft, which serves as the inlet duct passage to the impeller. This arrangement increases reliability with well-supported impeller blades and reduces risk of blade damage due to contacting the top pump housing. The device is mechanically robust and easy to manufacture. The hollow interior of the RSP

transfers momentum to the passing fluid, which may aid the pumping process by inducing circumferential momentum at the inlets of the impeller blades.

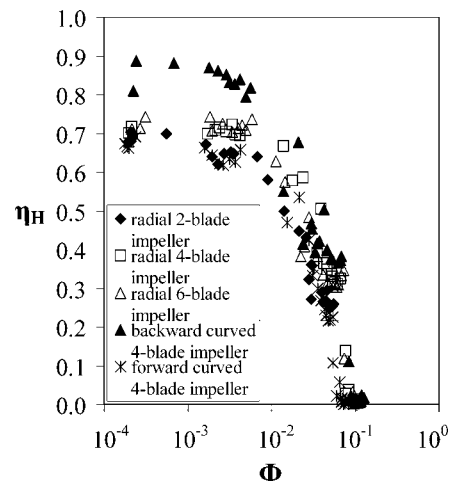


Fig. 12 Hydraulic efficiency for the different impeller configurations as dependent nondimensional volumetric flow rate. Data are taken with impeller rotational speeds from 1530 to 15,300 rpm.

Table 2 Slip factors obtained from Eqs. (5) and (9) for various impellers

Impeller configuration	Slip factor (σ)
Radial 2-blade impeller	0.384
Radial 4-blade impeller	0.621
Radial 6-blade impeller	0.715
Backward-curved 4-blade impeller	0.622
Forward-curved 4-blade impeller	0.638

The tested pump impeller is 2.38 mm in diameter, the height of the impeller blades is 380 μm , and the impeller speed varies from 1530 to 15,300 rpm. The bored hole in the impeller shaft is 1.168 mm in diameter, as seen in Fig. 1. Similar pressure versus flow rate slope characteristics for all impeller designs, and the differences relative to macroscale arrangements, provide evidence that the trends of these data are influenced by viscous forces, as well as by the impeller design (backward-curved, forward-curved, radial blades). Centrifugal-inertial forces also play an important role, since greater centrifugal forces are obtained at higher impeller rotational speeds, which generally increase pumping head magnitudes. By keeping the rotational speed constant and changing the flow rate by varying the outlet tube diameter and outlet valve, the pumping head is shown to decrease with increased flow rate. Such behavior is associated with overall impeller behavior and with increased hydrodynamic losses as flow rate increases.

The hydraulic efficiency changes by as much as 22% between different impeller configurations (i.e., the radial two-blade and backward curved four-blade impeller designs) for the same flow rate. The hydraulic efficiency for all impeller configurations decreases significantly for flow rates of >5 ml/min, or for $\Phi > 0.014$, due to the increased hydrodynamic losses. The highest hydraulic efficiency of 0.87 is produced by the backward-curved four-blade impeller with a rotational speed of 15,300 rpm and a flow rate of 0.12 ml/min, or a Φ value of 2.35×10^{-4} .

The performance of the RSP shows that pressure rise and flow rate increase for a constant outlet tubing diameter as rotational speed increases. The present millimeter-scale RSP produces flow rates up to 64.9 ml/min. Figure 13 shows the maximum flow rate for the RSP relative to the flow rate of several other different micropumps [2–13,17–27]. The typical size is defined as the membrane diameter, or the pumping chamber width. The flow rate of the RSP is larger than many other micropumps of similar size, as seen in Fig. 13, which generally reach flow rates only up to about 16 ml/min. Figure 14 shows the pressure and flow rate of the backward-curved four-blade impeller at different rotational speeds relative to the maximum flow rate and maximum pressure

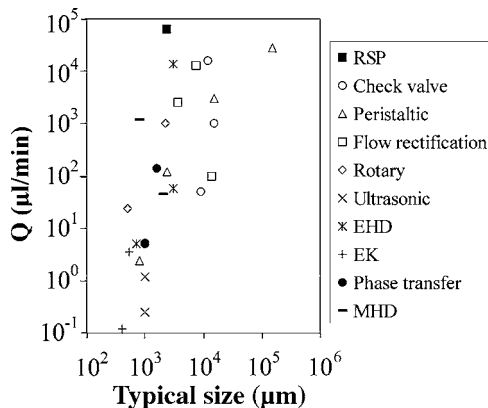


Fig. 13 Flow rate and typical size for various micropumps. Typical size is defined by the impeller diameter, diaphragm diameter, or pumping channel width [2–13,17–27].

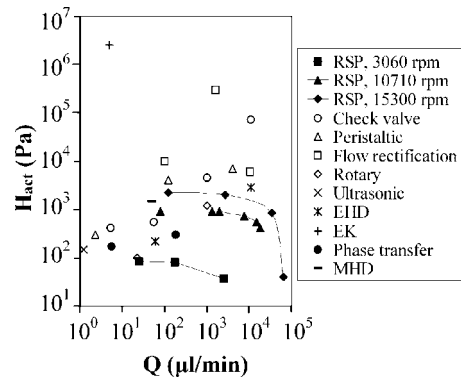


Fig. 14 Pressure-rise and flow-rate data for various micropumps. For all points other than the RSP, the data corresponds to the maximum flow rate and maximum pressure. The data shown for the RSP is for the backward-curved four-blade impeller [2–9,11,13,17–20,23–26].

rise of other micropumps [2–9,11,13,17–20,23–26]. Larger-scale versions of the rotary shaft pump may be ideal for applications in blood pumping, and ventricle assist devices [28–30], chemical analysis systems, drug delivery, and electronics cooling. Smaller-scale versions are ideally suited for chemical analysis systems, μ -TAS, and drug delivery.

Acknowledgment

Work presented in this paper was supported by the National Science Foundation (NSF) through the IGERT Program, Grant Number DGE 9987616.

Nomenclature

- C_{u1} = tangential component of the absolute fluid velocity at the impeller blade inlet
- C_{u2} = tangential component of the absolute fluid velocity at the impeller blade outlet
- $C_{u2,i}$ = ideal value of tangential component of the absolute fluid velocity at the impeller blade inlet
- D = inner diameter of tubing
- D_2 = outer diameter of impeller
- g = gravitational constant
- h = height of blades
- H = pumping head
- H_{th} = theoretical head or Euler head
- H_{act} = actual measured head between pump inlet and outlet
- n = number of impeller blades
- ΔP = pressure rise across pump measured between pump inlet and outlet
- Q = volumetric flow rate
- T = motor torque
- U_1 = blade speed at the impeller inlet
- U_2 = blade speed at the impeller outlet
- $v_{\theta s}$ = slip velocity

Greek Symbols

- α = impeller inlet swirl factor
- β = blade angle
- β_1 = inlet blade angle measured relative to the tangential direction
- β_2 = outlet blade angle measured relative to the tangential direction
- η_H = hydraulic efficiency
- ρ = density
- σ = slip factor

- Φ = nondimensional volumetric flow rate,
 $\Phi = 4Q / \pi D_2^2 U_2$
- Ψ = nondimensional pump head, $\Psi = Hg / U_2^2$
- Ψ_{act} = nondimensional actual measured pump head
between pump and inlet and outlet
- Ψ_{th} = non-dimensional theoretical pump head or Euler head

References

- [1] Nhuyen, N.-T., and Wereley, S. T., 2002, *Fundamentals and Applications of Microfluidics*, Artech House, Norwood, pp. 292–337.
- [2] Olsson, A., Steeme, G., and Steeme, E., 1995, "A Valve-Less Planar Fluid Pump With Two Pump Chambers," *Sens. Actuators, A* **47**(2), pp. 549–556.
- [3] Tsia, J. H., and Lin, L., 2002, "A thermal Bubble Actuated Micro Nozzle-Diffuser Pump," *J. Microelectromech. Syst.* **11**(6), pp. 665–668.
- [4] Nguyen, N. T., and Huang, X. Y., 2001, "Miniature Valveless Pumps Based on Printed Circuit Board Technique," *Sens. Actuators, A* **88**(2), pp. 104–111.
- [5] Benard, W. L., Kahn, H., Heuer A. H., and Huff, M. S., 1998, "Thin Film Shape-Memory Alloy Actuated Micropumps," *J. Microelectromech. Syst.* **7**(2), pp. 245–251.
- [6] Meng, E., Wang, X.-Q., Jak, H., and Tai, Y.-C., 2000 "A Check-Valved Silicone Diaphragm Pump," *Proc of MEMS '00, 13th Int. Workshop Micro ElectroMechanical Systems*, Japan, Jan. 23–27, IEEE, New York, pp. 23–27.
- [7] Gass, V., Van der Schoot, G. H., Jeanneret, S., and DeRooij, N. F., 1994, "Integrated Flow-Regulated Silicon Micropump," *Sens. Actuators, A*, **43**, pp. 335–338.
- [8] Saggere, L., Hagedorn, N. W., Roberts, D. C., Li, H. Q., Steyn, J. L., Turner, K., Carretero, J. A., Yaglioglu, O., Su, Y. H., Mlcak, R., Spearing, S. M., Breuer, K. S., and Schmidt, M. A., 2000, "Design, Fabrication, and Testing of a Piezoelectrically Driven High Flow Rate Micro-Pump," *Proc. of 12th IEEE Int. Symp. on Applications of Ferroelectrics*, July-Aug, IEEE, New York, Vol. 1, pp. 297–300.
- [9] Richter, A., Plettner, A., Hofmann, K. A., and Sandmaier, H., 1991, "A Micromachined Electrohydrodynamic (EHD) Pump," *Sens. Actuators, A* **29**, pp. 159–168.
- [10] Fuhr, G., Hagedorn, R., Muller, T., Benecke, W., and Wagner, B., 1992, "Microfabricated Electrohydrodynamic (EHD) Pumps for Liquids of Higher Conductivity," *J. Microelectromech. Syst.* **1**(3), pp. 141–146.
- [11] Ahn, S. H., and Kim, Y. K., 1998, "Fabrication and Experiment of a Planar Micro Ion Drag Pump," *Sens. Actuators, A* **70**, pp. 1–5.
- [12] Furuya, A., Shimokawa, F., Matsuura, T., and Sawada, R., 1996, "Fabrication of Fluorinated Polyimide Microgrids Using Magnetically Controlled Reactive Ion Etching (MC_RIE) and Their Applications to a Ion Drag Integrated Micropump," *J. Micromech. Microeng.* **6**, pp. 310–319.
- [13] Zeng, S., Chen, C. H., Mikkelsen, J. C., and Santiago, J. G., 2000, "Fabrication and Characterization of Electrokinetic Micro Pumps," 7th Intersociety Conf. on Thermal and Thermomechanical Phenomena in Electronic Systems, CPMT/IEEE, Las Vegas, 2, pp. 31–36.
- [14] Hainan, C., Ahaoying, Z., Yong, L., Xiongying, Y., and Yihua, Y., 1997, "A Novel Centrifugal Miniature Pump and Its Medical Application," *Proc. of the 1997 Int. Symp. on Microelectronics and Human Science*, Oct., IEEE, New York, pp. 115–117.
- [15] Kilani, M., Galambos, P., Haik, Y., and Chen, C. J., 2003, "Design and Analysis of a Surface Micromachined Spiral-Channel Viscous Pump," *ASME J. Fluids Eng.* **125**(2), pp. 339–344.
- [16] Sen, M., Wajerski, D., and Gad-el-Hak, M., 1996, "A Novel Pump for MEMS Applications," *ASME J. Fluids Eng.* **118**(3), pp. 624–627.
- [17] Ahn, C. H., and Allen, M. G., 1995, "Fluid Micropumps Based on Rotary Magnetic Actuators," *Proc. of MEMS 1995*, Jan.–Feb., IEEE, New York, pp. 408–418.
- [18] Dopfer, J., Clemens, M., Ehrfeld, W., Jung, S., Kamper, K.-P., and Lehr, H., 1997, "Micro Gear Pumps for Dosing of Viscous Fluids," *J. Micromech. Microeng.* **7**(2), pp. 230–232.
- [19] Mizoguchi, H., Ando, M., Mizuno, T., Takagi, T., and Nakajima, N., 1992, "Design and Fabrication of Light Driven Micropump," *Proc. of MEMS '92, 5th IEEE Int. Workshop MEMS*, Germany, Jan. 25–28, IEEE, New York, pp. 31–36.
- [20] Grosjean, C., and Tai, Y. C., 1999, "A Thermopneumatic Peristaltic Micropump," *Proc. of Transducer '99, 10th Int. Conf. on Solid State Sensors and Actuators*, Japan, June 7–10, IEEE, New York, pp. 1776–1779.
- [21] Cabuz, C., Herb, W. R., Cabuz, E. I., and Lu, S. T., 2001, "The Dual Diaphragm Pump," *Proc. of MEMS '01, 14th IEEE Int. Workshop MEMS*, Switzerland, Jan. 21–25 IEEE, New York, pp. 519–522.
- [22] Luginbuhl, Ph., Collins, S. D., Racine, G. A., Grettillat, M. A., de Rooij, N. F., Brooks, K. G., and Setter, N., 1997, Flexural-Plate-Wave Actuators Based on PZT Thin Films," *Proc. of MEMS '97*, Jan, 1997, IEEE, New York, pp. 327–332.
- [23] Miyazaki, S., Kawai, T., and Araragi, M., 1991, "A Piezoelectric Pump Driven by a Flexural Progressive Wave," *Proc. of MEMS '91, 4th Int. Workshop MEMS*, Japan, Jan. 30–Feb. 4, IEEE, New York, pp. 283–288.
- [24] Takagi, H., Maeda, R., Ozaki, K., Parameswaran, M., and Mehta, M., 1994, "Phase Transformation Type Micropump," *Proc. of Int. Symp. on Micro Machine and Human Sciences*, Japan, Oct., IEEE, New York, pp. 199–202.
- [25] Geng, X., Yuan, H., Oguz, H. N., and Prosperetti, A., 2001, "Bubble-Based Micropump for Electrically Conducting Liquids," *J. Micromech. Microeng.* **11**, pp. 270–276.
- [26] Hatch, A., Kamholz, A. E., Holman, G., Yager, P., and Bohringer, K. F., 2001, "A Ferrofluidic Magnetic Micropump," *J. Microelectromech. Syst.* **10**(2), pp. 215–221.
- [27] Huang, L., Wang, W., Murphy, M. C., Lian, K., and Ling, Z. G., 2000, "LIGA Fabrication and Test of a DDC Type Magnetohydrodynamic (MHD) Micropump," *Microsc. Res. Tech.* **6**, pp. 235–240.
- [28] Shen, J. X., Tseng, K. J., Vilathgamuwa, D. M., and Chan, W. K., 2000, "A Novel Compact PMSM with Magnetic Bearing for Artificial Heart Application," *IEEE Trans. Ind. Appl.* **36**(4), pp. 1061–1068.
- [29] Wan, S. and Tseng, K. J., 2001, "Novel Bearingless Centrifugal Blood Pump," *Proc. of 4th Int. Conf. on Power Electronics and Drive Systems*, Denpasar, IEEE, New York, Vol. 2, pp. 743–748.
- [30] Nishimura, K., Park, C.-H., Akamatsu, T., Yamada, T., and Ban, T., 1996, "Development of a Magnetically Suspended Centrifugal Pump as a Cardiac Assist Device for Long-Term Application," *ASAIO J.* **42**(1), pp. 68–71.
- [31] Karniadakis, G. E., Beskok, A., 2002, *Micro Flows, Fundamentals and Simulation*, Springer, New York, pp. 1–31.
- [32] Blanchard, D., Ligrani, P., and Gale, B., 2004, "Rotary Centrifugal and Viscous Micropumps", US Patent Office, Application No. PCT/US2004/028890, International Publication No. WO2005/024230 A2 March 17, 2005 (pending).
- [33] Fox, R. W., and McDonald, A. T., 1998, *Introduction to Fluid Mechanics*, 5th Edition, Wiley, New York, pp. 493–522.
- [34] Gorla R. S. R. and Khan, A. A., 2003, *Turbomachinery, Design and Theory*, Marcel Dekker, New York, pp. 47–90.
- [35] Brennan, C. E., 1995, *Hydrodynamics of Pumps*, Oxford University Press, Cary, NC.
- [36] Wiesner, F. J., 1967, "A Review of Slip Factors for Centrifugal Impellers," *ASME J. Eng. Power* **89**, pp. 558–572.
- [37] Stodola, A., 1927, *Steam and Gas Turbines*, McGraw-Hill, New York, Vols I and II.
- [38] Stanitz, J. D., 2001, "Some Theoretical Aerodynamic Investigations of Impellers in Radial and Mixed Flow Centrifugal Compressors," *ASME J. Appl. Mech.*, **74**(4), pp. 473–497.
- [39] Paeng, K. S., and Chung, M. K., 2001, "A New Slip Factor for Centrifugal Impellers," *Proc. Inst. Mech. Eng., Part A* **215**(5), pp. 645–649.
- [40] Moffat, R. J., 1982, "Contributions to the Theory of Single-Sample Uncertainty Analysis," *ASME J. Fluids Eng.* **104**, pp. 250–260.